Biomaterials Advances 178 (2026) 214440

Contents lists available at ScienceDirect

Biomaterials Advances

journal homepage: www.journals.elsevier.com/materials-science-and-engineering-c

Beeswax-enriched tricalcium phosphate/hydroxyapatite/sodium alginate/thymol 3D-printed scaffolds for application in bone tissue engineering

Martinho J. Francisco [a,b], Cátia S.D. Cabral [a], Paula Ferreira [c,d,e], Ilídio J. Correia [a,b,c,*], André F. Moreira [a,f,*]

[a] RISE-Health, Departamento de Ciências Médicas, Faculdade de Ciências da Saúde, Universidade da Beira Interior, Av. Infante D. Henrique, 6200-506 Covilhã, Portugal
[b] AEROG-LAETA, Aerospace Sciences Department, Universidade da Beira Interior, Covilhã, Portugal
[c] University of Coimbra, CERES – Centro de Engenharia Química e Recursos Renováveis para a Sustentabilidade, Department of Chemical Engineering, Coimbra 3030-790, Portugal
[d] Polytechnic Institute of Coimbra, Applied Research Institute, Rua da Misericórdia, Lagar dos Cortiços – S. Martinho do Bispo, Coimbra 3045-093, Portugal
[e] Research Centre for Natural Resources, Environment and Society (CERNAS), Polytechnic Institute of Coimbra, Coimbra 3045-601, Portugal
[f] BRIDGES - Biotechnology Research, Innovation, and Design of Health Products, Polytechnic of Guarda, Av. Dr. Francisco Sá Carneiro, 50, 6300-559 Guarda, Portugal

ARTICLE INFO

Keywords:
3D scaffolds
Beeswax
Bone tissue engineering
Thymol
Antibacterial scaffolds
Composite materials

ABSTRACT

Tissue engineering, particularly bone tissue engineering (BTE), continues to pose significant challenges to modern medicine. In this work, a rapid prototyping technique was explored to create 3D scaffolds using a Fab@Home 3D-Plotter extruder. For that purpose, a novel composite mixture containing tricalcium phosphate (TCP), hydroxyapatite (HAp), sodium alginate (SA), beeswax (BW), and thymol (TM) was formulated. BW and TM resulted in 3D scaffolds with rougher surfaces and moderate hydrophilic profiles, properties crucial for mediating cell adhesion and proliferation. Moreover, the 3D scaffolds containing BW displayed a significant increase in compressive strength and Young modulus, being comparable to those exhibited by trabecular bone. TM loading prevented the establishment of *Staphylococcus aureus* and *Escherichia coli* infections, inhibiting bacterial adhesion and proliferation at the scaffolds' surface. Additionally, the cytocompatibility of the scaffolds was confirmed over 21 days, with the adhesion and proliferation of Human osteoblasts (hOB) at the scaffold's surfaces. Simultaneously, calcium and phosphate ions accumulated at the scaffolds' surface, forming apatite crystals. Therefore, this improved composite mixture showed promising results for being applied in BTE, not only facilitating hOB cell adhesion and proliferation but also avoiding bacterial infection, addressing a critical challenge in implant-based therapies.

1. Introduction

Bone tissue engineering (BTE) is a multidisciplinary approach that seeks to replicate and enhance the body's natural processes to generate bone tissue through the integration of biomaterials, cells, and bioactive factors [1,2]. As a response to the limitations of traditional bone grafts, BTE aims to guide the complex and highly regulated physiological mechanisms involved in bone repair and formation [3–6]. By mimicking the native bone environment, BTE facilitates the recruitment, proliferation, and differentiation of osteogenic cells, ultimately promoting the formation of structurally and functionally viable bone tissue. Particularly, BTE aims to develop three-dimensional (3D) solutions that can replicate the characteristics of native bone, namely the inorganic (i.e., hydroxyapatite) and the organic (e.g., collagen type I, bone cells, and non-collagenous proteins) phases [7–11]. To accomplish that, researchers have been using various material combinations, including natural or synthetic polymers, ceramics, metals, and other composite materials [12,13].

Herein, a novel 3D scaffold was fabricated through a rapid prototyping technique, using the Fab@Home 3D-Plotter extruder via a top-down approach. For that purpose, a novel composite mixture comprising tricalcium phosphate (TCP), hydroxyapatite (HAp), sodium alginate (SA), beeswax (BW), and thymol (TM) was optimized. TCP is widely used in BTE due to its biocompatibility, biodegradability, and

* Corresponding authors at: RISE-Health, Departamento de Ciências Médicas, Faculdade de Ciências da Saúde, Universidade da Beira Interior, Av. Infante D. Henrique, 6200-506 Covilhã, Portugal.
E-mail addresses: icorreia@ubi.pt (I.J. Correia), afmoreira@fcsaude.ubi.pt, afmoreira@ipg.pt (A.F. Moreira).

https://doi.org/10.1016/j.bioadv.2025.214440
Received 24 January 2025; Received in revised form 31 July 2025; Accepted 1 August 2025
Available online 5 August 2025

osteoconductivity. Additionally, TCP is more affordable than hydroxyapatite and presents a higher rate of degradation, with its degradation products being absorbed by the cells and used in the formation of bone tissue [9,14]. HAp has been studied due to its ability to enhance physicochemical properties such as porosity, which positively contribute to the osteoprogenitor cells' adhesion, proliferation, and differentiation [3]. Moreover, HAp is also known to stimulate the production of osteogenic growth factors (e.g., Bone Morphogenic protein (BMPs)), and contribute to the increase of alkaline phosphatase (ALP) activity in mesenchymal stem cells (MSCs) [15,16]. As for the organic components, SA is a low-cost, biodegradable, biocompatible, low immunogenic, and highly viscous natural polymer extracted from the cell walls of brown algae, including *Laminaria hyperborea* and *Laminaria digitata* [17,18]. In addition, SA is soluble in water and can undergo ionotropic crosslinking in the presence of bivalent cations such as calcium (Ca^{2+}) ions, which is essential for maintaining the scaffolds' structure [19]. However, the application of SA in BTE can be hindered by its poor mechanical resistance and excessive swelling [20,21].

On this note, recent advancements have emphasized the bioactive potential of natural compounds and polymer combinations, especially plant secondary metabolites (e.g., flavonoids and monoterpenes), and honeybee products, such as honey, propolis, and beeswax, for improving the effectiveness of tissue engineering solutions [22–24]. These natural bioactive substances may not only present antimicrobial activity but also the capacity to moderate hydrophilicity, contribute to osteoinduction, and control the inflammatory response [22,23,25]. Thymol (2-isopropyl-5-methylphenol) is a monoterpene phenolic compound mainly extracted from thyme (*Thymus vulgaris* L.) and oregano (*Origanum vulgare* L.) essential oils. It is well-known for its antimicrobial, anti-inflammatory, and antioxidant properties [26,27]. In fact, TM has been explored to confer bactericidal and anti-inflammatory capacity to different biomaterials such as electrospun membranes, films, and hydrogels [28–31]. Due to its easy incorporation and high bactericidal capacity, TM is considered an effective candidate against antibiotic-resistant bacteria, which are known to cause biofilm formation on implanted bone scaffolds [23,29,32,33]. BW is a naturally hydrophobic and biocompatible compound produced by honeybees' (*Apis mellifera*) glands [34]. Its natural composition reduces the risk of adverse immune reactions, which categorizes BW as GRAS (Generally Recognized as Safe) by the FDA, an essential feature for a biomaterial aimed to be applied in the biomedical field [35]. BW has an intricate and ideal crystalline structure, contributing to its primary function as a support construct for the honeycomb [36,37]. Around 300 compounds can be found in BW, in which fatty alcohols represent almost 1 %, hydrocarbons 12–16 %, free fatty acids 12–14 %, fatty acid esters around 67 %, and honeycomb substances such as pollen, propolis, and some floral constituents make up the remaining components [24,38]. BW has been extensively used as a food additive, a thickener, an emulsion agent, and a drug release control agent in food, pharmaceutical, and cosmetic industries [36–39]. Furthermore, bone wax (a mixture of beeswax, isopropyl palmitate, and softening agents) has been used for a long time in osteotomy operations to control bleeding [40]. In recent BTE studies, researchers have used BW as a bio-ointment (to improve formulations viscosity), as an encapsulating agent (to control drug release in hydrogels/emulsions), and as a coating agent (which prevents corrosion of metal alloy grafts) to improve bone tissue formation [35,41–44]. Herein, BW was explored, for the first time, as part of the organic phase in 3D-printed scaffolds for bone generation, evaluating its impact on the layer-by-layer material deposition and the 3D-printed scaffolds' mechanical stability and bioactivity.

2. Materials and methods

2.1. Materials

Alizarin Red S (ARS), Dulbecco's modified Eagle's medium (DMEM-F12), di-Potassium hydrogen phosphate trihydrate ($HK_2O_4P.3H_2O$), glutaraldehyde 2 % (*v*/v), hydrochloric acid (HCl), hydroxyapatite (HAp), LB Broth, resazurin, sodium alginate (SA), sodium hydroxide (NaOH), thymol (TM), triton X-100, and trypsin were acquired from Sigma-Aldrich (Sintra, Portugal). Acetic acid was purchased from Pronalab (Barcelona, Spain). Double-deionized and filtered water was obtained using a Milli-Q Advantage A10 ultrapure Water Purification System (0.22 μm filtered; 18.2 MΩ/cm at 25 °C). Ethanol 99.5 % (EtOH) was acquired from Aga (Prior Velho, Portugal). Ethyl acetate, tris-base, and tris-buffered saline (TBS) were obtained from Fisher Scientific (Porto Salvo, Portugal). Fetal bovine serum (FBS) was obtained from Biochrom AG (Berlin, Germany). Lysozyme from the chicken egg was purchased from Alfa Aesar (Haverhill, MA, USA). Magnesium chloride hexahydrate ($MgCl_2.6H_2O$), potassium chloride (KCl), and sodium sulfate anhydrous (Na_2SO_4) were purchased from Labkem (Barcelona, Spain). Normal human osteoblast (hOB; 406-05f) cryopreserved cells were obtained from Cell Applications, Inc. (San Diego, USA). *Staphylococcus aureus* clinical isolate (*S. aureus*; ATCC 25923) and *Escherichia coli DH5α* (*E. coli*) were used to evaluate the antimicrobial properties of scaffolds. Propidium Iodide was acquired from Life Technologies (Maryland, USA). Tricalcium phosphate (TCP) was obtained from Panreac (Barcelona, Spain). Sodium bicarbonate ($NaHCO_3$) was purchased from Labchem (Santo Antão do Tojal, Portugal). White Beeswax (BW) was acquired from GUINAMA (Valencia, Spain).

2.2. Methods

2.2.1. Fabrication of the 3D scaffolds

The formulations were prepared using different compositions (Table 1). Briefly, SA was dissolved in 4.4 mL double-deionized and filtered water (0.22 μm filtered; 18.2 MΩ/cm at 25 °C) and then homogenized for 10–15 min with an X10/25 Ultra-Turrax 8G. Then, TCP and HAp, in a ratio of 4:1, were mixed with the SA solution and homogenized for 15 min in X10/25 Ultra-Turrax 8G. A BW 10 % (*w*/*v*) solution was prepared using 3.6 mL ethyl acetate as solvent, under magnetic agitation at 80 °C, for 45 min. Afterward, TM-BW solutions were prepared at a final TM concentration of 0.016 % or 0.033 %. Subsequently, the BW-TM solution was added to the previous SA/TCP-HAp mixture and homogenized for 10 min. After homogenization, the formulations were dried at 50 °C for 3 h. The layer-by-layer 3D printing of the composite mixtures was performed in a Fab@Home 3D printer. For that purpose, the composite mixtures were homogenized and loaded into a syringe (10 cc Luer Lock) with an 18G nozzle, which was then mounted in the Fab@Home 3D printer. Then, the printing parameters (Table S1) were adjusted for each composite mixture, and 3D-printed formulations were produced by layer-by-layer extrusion, following a 3D CAD model of a general model unit according to a previous work [45]. The 3D structure comprised a 13 mm × 13 mm × 13 mm cube, with a porous structure and several layers angled at 45° with the underlying layer (0°–45°–90°–135°). The layer rotation mimics the

Table 1
Summary of the composition of the mixtures corresponding to twelve scaffolds/formulations.

	Inorganic/Organic Ratio				
	70 (4:1)		30 (2:1)		
	TCP (g)	HAp (g)	SA (g)	BW (g)	TM (g)
TCP/SA (T)	2.52	–	1.08	–	–
TCP/SA/BW (TB)	2.52	–	0.72	0.36	–
TCP-HAp/SA/BW (THB)	2.02	0.50	0.72	0.36	–
TCP-HAp/SA/BW-TM5 (TM5)	2.02	0.50	0.72	0.36	0.06
TCP-HAp/SA/BW-TM10 (TM10)	2.02	0.50	0.72	0.36	0.12
Density (g/ml)	0.82				

collagen deposition in natural lamellar bone, namely the rotation of collagen fibers between adjacent lamellae [46]. Then, the crosslinking of the SA chains was promoted by soaking the scaffolds in a $CaCl_2$ solution (5 % *v*/v) for 24 h. Finally, the 3D-printed scaffolds were recovered and dried at 50 °C for 3 days.

2.2.2. Morphological characterization of the 3D scaffolds

Scanning Electron Microscopy (SEM) was used to analyze the 3D scaffolds' macroporosity, surface, and morphology. Samples were affixed to aluminum stubs with Araldite glue and coated with gold using a Quorum Q150RES sputter coater (Quorum Technologies, UK). Once this process was completed, image acquisition was performed in a Hitachi S-3400 N scanning electron microscope (Japan) at 20 kV acceleration voltage. Additionally, sectional images of the scaffolds' cryo-fracture were also obtained. This process involved soaking the samples in liquid nitrogen for 30 s, followed by the scaffolds' fracture at the center.

2.2.3. Physicochemical characterization of the scaffolds

2.2.3.1. Attenuated total reflectance-Fourier transform infrared spectroscopy (ATR-FTIR). The scaffolds' chemical composition was analyzed using ATR-FTIR spectroscopy. For this purpose, each scaffold formulation was first crushed into powder and then placed on a Nicolet iS10 FTIR Spectrophotometer (Thermo Scientific, Waltham, MA, USA). All spectra were recorded with an average of 64 scans, at a resolution of 4 cm^{-1}, and in the 600–3600 cm^{-1} range, adapting a protocol previously established in our group [47]. The spectra of the raw materials used to create the composite mixture were also acquired for comparison.

2.2.3.2. Energy-dispersive spectroscopic analysis (EDS). The 3D scaffolds' elemental composition and surface mineralization were analyzed using EDS. Briefly, the samples were freeze-dried for 3 h, then placed on aluminum stubs, and analyzed using an XFlash Detector 5010 (Bruker Nano, Germany).

2.2.4. Mechanical characterization of the scaffolds

The 3D scaffolds' ($n = 3$) mechanical properties were evaluated under wet and dry conditions. For that purpose, scaffolds were submerged in TBS at a pH of 7.4 overnight. After that process, both dry and wet scaffolds underwent compression tests to analyze their mechanical behavior. The assay was performed at RT with a load cell of 5 kN and a crosshead speed of 2 mm/min, using a Shimadzu AG-X tensile testing machine (Tokyo, Japan) [48].

The compressive strength (C_s) was calculated using Eq. (1):

$$C_s = \frac{F}{w \times l} \tag{1}$$

In this context, F is the load at the time of fracture, while w and l stand for the width and length of the scaffolds, respectively.

Young's modulus (*YM*) was determined using the stress-strain relationship, as demonstrated in Eq. (2):

$$YM = \frac{C_s}{H_d} \tag{2}$$

where C_s represents the scaffold compressive strength, and H_d is the height deformation at maximum load.

Energy absorption (E_a) was calculated by integrating the force-displacement curve, according to Eq. (3):

$$E_a = \int_0^{\varepsilon_i} \sigma_i d\varepsilon \tag{3}$$

where σ_i is the stress value at ε_i strain in the strain-stress curve.

2.2.5. 3D scaffolds' porosity evaluation

The scaffolds' ($n = 5$) porosity was analyzed using the liquid displacement method as previously reported in the literature [49]. The samples were weighed, soaked in EtOH for 48 h, and reweighed. The EtOH was chosen as a solvent due to its capacity to infiltrate the scaffolds' structure without causing swelling or shrinkage [48]. The sample's overall porosity was determined using Eq. (4):

$$Porosity\ (\%) = \frac{W_w - W_d}{D_{EtOH} \times V_{scaffold}} \times 100 \tag{4}$$

where W_w and W_d represent the wet and dry scaffolds' weights, respectively. D_{EtOH} corresponds to EtOH density at RT, and the $V_{scaffold}$ refers to the scaffolds' volume.

2.2.6. Characterization of the scaffolds' swelling profile

The 3D scaffolds' swelling was characterized using cell culture media, adapting a method described in the literature [48]. Briefly, the 3D scaffolds ($n = 5$) were incubated with DMEM-F12 (pH 7.4), under stirring (20 rpm) at 37 °C, for approximately 72 h. The scaffolds were then recovered, weighed, and re-immersed in the DMEM-F12 solution at predetermined intervals.

The swelling was calculated using Eq. (5):

$$Swelling\ (\%) = \left(\frac{W_t - W_0}{W_0} \right) \times 100 \tag{5}$$

where W_t corresponds to the final weight of the scaffolds, and W_o indicates the initial weight.

2.2.7. Evaluation of the scaffolds' hydrophobic/hydrophilic character

The sessile drop method was used to optically determine the contact angle between a liquid and a solid surface, allowing the determination of the scaffolds' hydrophilicity. In this method, a 10 μL drop of deionized water was automatically dispensed onto the surface of the sample, and the resulting contact angle was measured using a Dataphysics OCA 20 contact angle analyzer (Dataphysics Instruments, Filderstadt, Germany). Multiple measurements were taken at various points on the surface of the scaffolds to calculate the mean static water contact angle (WCA) and its standard error.

2.2.8. Mineralization assay

The scaffolds' mineralization capacity was evaluated in a simulated body fluid (SBF) solution, at 37 °C for 21 days. At different times, samples were collected and freeze-dried for 3 h. SEM was performed to visualize and characterize the apatite crystal layers. The formation of apatite crystals was also monitored by measuring the amount of calcium and phosphorus elements present at the scaffold's surface via EDS analysis. The SBF was prepared at pH 7.4 and with the following concentration of ions: 142.0 mM Na^+, 5 mM K^+, 1.5 mM Mg^{2+}, 2.5 mM Ca^{2+}, 147.8 mM Cl^-, 4.2 mM HCO_3^-, 1.0 mM HPO_4^{2-}, and 0.5 mM SO_4^{2-} [50].

2.2.9. Evaluation of the scaffolds' biodegradation profile

The degradation profile of the samples was monitored in the presence or absence of an enzyme. Briefly, the 3D scaffolds were immersed in DMEM-F12 medium, with or without lysozyme (13.6 mg/L), and incubated for 14 days at 37 °C under stirring [48]. Then, the scaffolds were removed from the solution at specific times, frozen at −80 °C, freeze-dried for 3 h, and reweighed.

The weight loss percentage at each time point was determined using Eq. (6):

$$Weight\ loss\ (\%) = \left(\frac{W_i - W_f}{W_i} \right) \times 100 \tag{6}$$

where W_i is the initial weight of the scaffold and W_f corresponds to the

weight of the scaffold at time t.

2.2.10. Biological characterization of the scaffolds

2.2.10.1. Assessment of hOB cells' viability and proliferation in contact with the scaffolds. The resazurin assay was used to characterize the 3D scaffolds' cytotoxic profile [51]. To accomplish that, scaffolds were broken into quarters and placed in 12-well plates, and then UV light was used to sterilize them for 1.5 h. After that process, hOB cells were cultured with the 3D scaffolds and incubated for 1, 3, 7, 14, and 21 days. At the respective time points, both scaffolds and the culture medium were removed, and cells were incubated in the dark with 550 μL of fresh medium containing resazurin (50 μL) for 4 h at 37 °C and 5 % CO_2. Subsequently, the resorufin fluorescence was measured using a Spectramax Gemini EM spectrofluorometer ($\lambda_{ex} = 560$ nm and $\lambda_{em} = 590$ nm; Molecular Devices LLC, CA, USA). Cells incubated without materials and cells incubated with 70 % EtOH were used as negative (K^-) and positive (K^+) controls, respectively.

2.2.10.2. Evaluation of cell adhesion to the scaffolds' surface. To analyze cell adhesion on the scaffolds' surface, hOB cells (50×10^3 cells/wells) were directly seeded onto them. The cells were then incubated for 1, 3, and 7 days. At each time point, the medium was removed, and the samples were fixed using 2.5 % (*v*/v) glutaraldehyde for 30 min. Afterward, the scaffolds were frozen at −80 °C, freeze-dried for 3 h, and SEM images were acquired (as described in Section 2.2.2.). Additionally, the hOB cells' adhesion and internalization were also monitored using Confocal Laser Scanning Microscopy (CLSM). The 3D scaffolds and hOB cells (50×10^3 cells/scaffold) were cultured using μ-Slide 8-well Ibidi imaging plates (Ibidi GmbH, Germany). Then, at each time point (1, 3, and 7 days), the samples were permeabilized using a Triton X-100 solution, and the cell nuclei were labeled with propidium iodide (PI) at 15 mM, for 15 min at RT. Subsequently, DMEM-F12 medium was used to wash the samples, followed by fixation with 2.5 % (*v*/v) glutaraldehyde for 15 min. Finally, a Zeiss LSM 710 laser scanning confocal microscope (Carl Zeiss SMT Inc., USA) was used to acquire consecutive z-stacks forming a 3D reconstruction, analyzed in Zeiss Zen 2010 [52].

2.2.10.3. Biomineralization assay. The scaffolds' capacity to promote calcium deposition by hOB cells was analyzed using the alizarin Red S (ARS) staining method following a protocol previously optimized [52]. For this purpose, multiple cell densities were seeded with the scaffolds ($n = 5$) in 12-well plates and incubated for 1, 3, 7, 14, and 21 days. Then, the samples were fixed with 4 % (*v*/v) formaldehyde for 1 h and stained with 1 mL of ARS (40 mM, pH = 4.1–4.3) for 1 h under agitation. Finally, samples were washed (2×) with deionized H_2O, and the calcium deposits were visualized by microscopic images.

2.2.10.4. Evaluation of the scaffolds' antibacterial activity. A modified Kirby-Bauer protocol was used to characterize the scaffolds' antibacterial activity, in which both Gram-positive and Gram-negative bacteria were tested, *S. aureus* and *E. coli*, respectively [47]. For this purpose, the bacteria at 1×10^6 CFU/mL (OD = 0.5) were cultured on the agar plates and incubated with the 3D scaffolds ($n = 3$) for 24 h at 37 °C. Afterward, the inhibition halos were photographed and measured using the ImageJ software. Moreover, bacterial growth on the 3D scaffolds' surface was also assessed by SEM analysis, after freeze-drying the samples according to the protocol described in Section 2.2.2.

Otherwise, the bacterial viability of *S. aureus* and *E. coli* was also determined using the resazurin assay and counting the colony-forming units [53]. For that purpose, 3D scaffolds were incubated with bacterial suspensions (1×10^5 CFU/mL in LB broth) in 12-well plates at 37 °C for 24 h. In the negative control (K^-) bacteria were cultured in LB broth only, whereas in the positive control (K^+), the bacteria were cultured in LB broth supplemented with antibiotic-antimycotic solution (containing 0.25 μg/mL amphotericin B, 100 U/mL penicillin, and 100 μg/mL streptomycin). After incubation, 100 μL of bacterial medium was collected from each well and mixed with 20 μL of 0.05 % (*w*/*v*) resazurin solution for 4 h in the dark (37 °C, 5 % CO_2). The resazurin reduction was determined by using a BioRad xMark microplate spectrophotometer (λex = 570 nm, λem = 600 nm). Furthermore, the remaining bacterial medium from the test groups was serially diluted in LB media, and 100 μL samples were plated on LB agar plates. The culture plates were incubated overnight at 37 °C, and the colonies were documented photographically [54–56].

2.2.11. Statistical analysis

Results were statistically analyzed using one-way analysis of variance (ANOVA) with the Newman-Keuls post hoc test. The data are presented as mean ± s.d., a *p*-value lower than 0.05 ($p < 0.05$) was considered statistically significant.

3. Results and discussion

3.1. Morphological characterization of the 3D scaffolds

The 3D scaffolds were produced layer-by-layer using a Fab@Home 3D printer, using an extrusion-based methodology [48,57]. Moreover, since bones are chemically composed of an inorganic (60–75 %) and organic (25–40 %) phase, all 3D scaffold formulations were created in a 70:30 ratio of inorganic-to-organic material. The final mixture was formulated using TCP, HAp, SA, and BW, with each material contributing to mimicking the bone properties. TCP and HAp were included, in a 4:1 ratio, to mimic the inorganic phase. TCP was chosen for its mechanical and osteogenic properties, while HAp can improve the porosity of the scaffolds and even lead to enhanced mechanical properties and osteoinductivity [48,58–60]. Meanwhile, the SA and BW organic phase was added to the formulations in a 2:1 ratio. SA is a natural, biocompatible, hydrophilic, and biodegradable polymer, making it ideal for mimicking the extracellular matrix [48]. On the other hand, BW's crystalline structure and hydrophobic character help honeybees to develop a stable and durable structure, which in this case was expected to control the scaffolds' wettability and mechanical performance under wet conditions [36]. Additionally, TM was impregnated in BW to confer antibacterial properties to the scaffolds against both Gram-positive and Gram-negative bacteria [61]. Macroscopic and SEM images were acquired after the 3D scaffolds' production to evaluate their structure and morphology. The macroscopic images (Fig. 1A) show that all formulations have similar characteristics in terms of dimensions and shapes, with minor variations in the layer arrangement. The paths of the T formulation appear flattened (Fig. 1A, Top View), while the paths of all other formulations remain slightly straighter. This can be explained by the absence of BW in these mixtures. The wax solidifies as the organic solvent evaporates, contributing to a straighter path upon layer deposition. Furthermore, in the SEM images (Fig. 1B), BW and TM formulations appear to present a rougher surface, which can offer a higher number of anchorage points essential for cell adhesion and proliferation [62] as well as protein absorption, as reported in the literature [63]. Fig. S1 further shows the arrangement and connection between the different layers that compose the scaffolds.

3.2. Physicochemical characterization of the scaffolds'

3.2.1. ATR-FTIR analysis

The scaffolds' chemical composition was analyzed using ATR-FTIR, as shown in Fig. 2. The TCP raw spectra (Fig. 2A) display a single characteristic peak at 1021 cm^{-1}, attributed to the P═O vibration, which can also be observed in HAp spectra. In the SA spectra, two peaks at 1404 and 1597 cm^{-1} can be observed corresponding to the C═O stretching of the carboxylate group, along with a band between 3000 and 3600 cm^{-1} attributed to alginate's G and M units [48]. Otherwise,

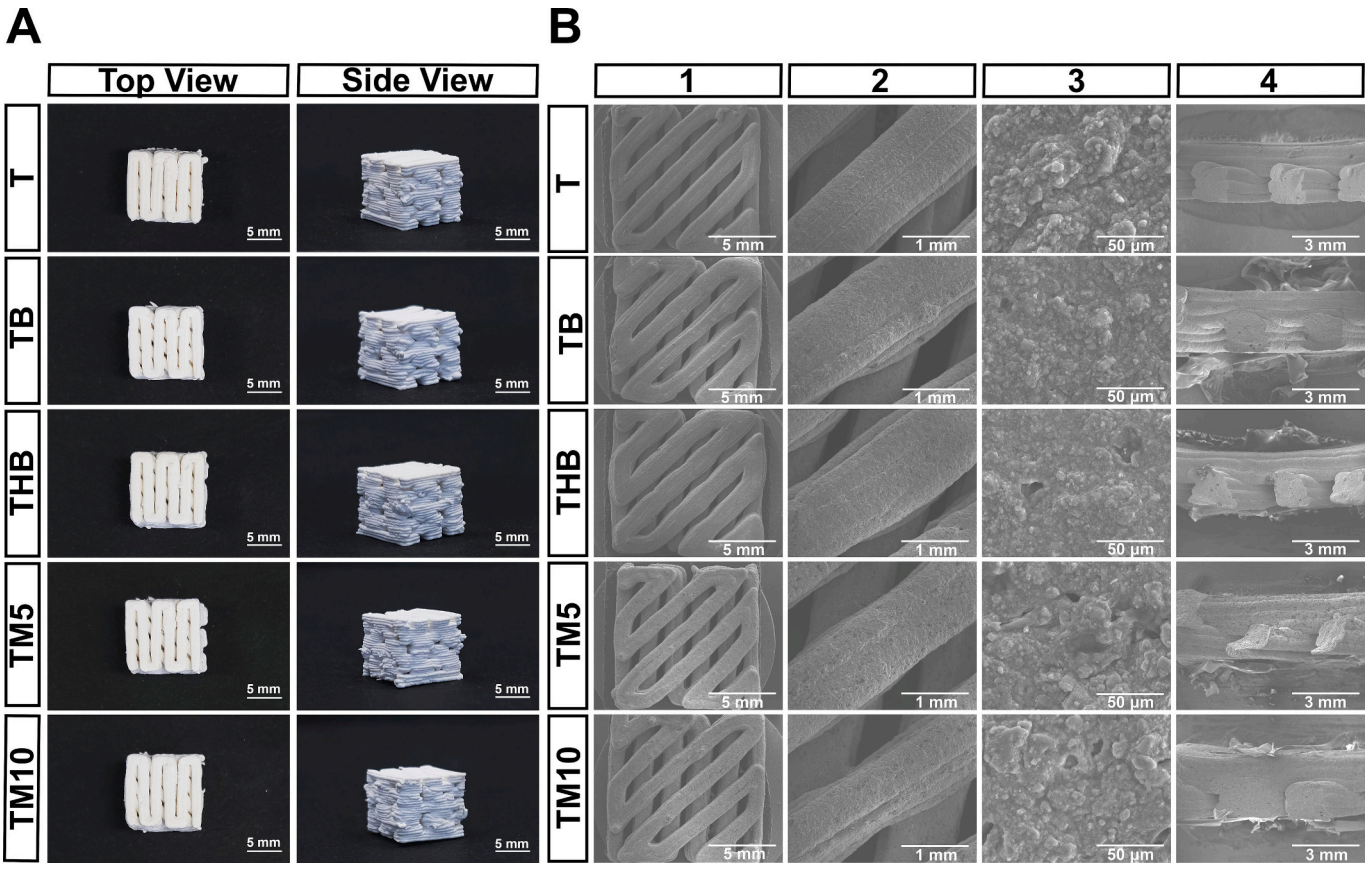

Fig. 1. Morphological evaluation of the produced scaffolds. Representative macroscopic images of the 3D scaffolds (top and side views) (A) and SEM images showing their morphology (B1), surface topography (B2 and B3), and cryofracture (B4).

the BW presented vibration bands at 2960–2820 cm^{-1}, attributed to the asymmetric CH_2 stretching. Moreover, the BW fingerprint zone (Fig. 2AI) in the 1800–900 cm^{-1} [64] region was also visible. In this region, it was possible to identify hydrocarbon scissor deformations at 1334 cm^{-1}, free fatty acids and esters at 1763 cm^{-1}, and 1179 cm^{-1} representing C═O stretching vibrations and C—H bending vibrations, respectively. Moreover, the TM spectra presented a peak at 1621 cm^{-1} from the C═C aromatic ring and the TM fingerprint zone (Fig. 2AII) at 1514–720 cm^{-1}, which contained peaks at 863 cm^{-1} (aromatic C—H out-of-plane bends), 1171 cm^{-1} (meta substitution), 1210 cm^{-1} (aromatic C—H in-plane bends), and 1485 cm^{-1} (C—H asymmetric/symmetrical bending) [65]. Additionally, it is possible to observe the presence of characteristic peaks of the corresponding raw material in the spectra of the different composite mixtures (Fig. 2B).

3.2.2. *EDS analysis*

The EDS analysis (Table S2) was conducted to determine the elemental composition of the 3D scaffolds. The results show a similar oxygen, phosphorus, and calcium content in all composite formulations. However, the carbon content increased with the addition of BW and TM to the different formulations. Moreover, the data in Table S3 indicated that the formulations exhibited a slightly higher Ca/P ratio (2.39–2.7) compared than native trabecular bone (1.3–2.2) [66].

3.3. *Mechanical properties of the scaffolds*

Optimal mechanical properties are crucial for scaffolds' performance in bone tissue formation. In this application, the biodegradable 3D scaffolds must provide temporary structural support while facilitating cell adhesion, proliferation, and the initial formation of hydroxyapatite crystals [48,67]. For this purpose, the 3D-printed scaffolds' compressive strength (C_s) and Young's modulus (YM) were tested in wet and dry conditions.

As stiffer scaffolds could lead to stress-shielding and lower stiffness fail to provide mechanical stability to the injury, the replacement biomaterial's mechanical properties should be similar to those of native bone tissue [68]. The results show that all formulations performed better in dry conditions (Fig. 3A and B). In this regard, it is possible to observe that adding BW to the mixtures (TB formulation) leads to an increase of approximately 25 % in C_s when compared to the T formulation, which was already optimized in a previous work in our group [48]. TB presents a value of approximately 25 MPa, whereas the T formulation is approximately 20 MPa. Additionally, to further increase the C_s of the TB formulation, HAp was added, resulting in a 28 % increase in C_s, surpassing the trabecular bone range (1–30 MPa). Moreover, no significant impact on the C_s value was observed with the addition of TM. However, the obtained results show a poorer performance of the 3D scaffolds under wet conditions, which can be attributed to the expansion of the polymeric matrix in response to the fluids. This can lead to swelling and loss of structural integrity, leading to decreased mechanical properties. The data obtained (Fig. 3A) demonstrate that adding BW helps minimize the loss of mechanical properties in wet conditions. While the control formulation loses almost 95 % of its C_s, incorporating BW into the scaffolds helps them retain over 30 % of their original resistance. This can be explained by the rapid solidification of the wax at RT and its internal crystalline structure, which helps bind the polymeric and ceramic phases in the composite mixture, acting as a mechanical adhesive [69]. Additionally, the hydrophobic nature of BW also plays a role in preventing increased swelling, as will be further discussed in Topic 3.6. Otherwise, the addition of BW almost doubled the scaffolds' energy absorption in a dry state, increasing from 1.35 ± 0.19 (T formulation) to 2.13 ± 0.67, 2.86 ± 0.51, 2.41 ± 0.10, and 2.81 ± 0.43

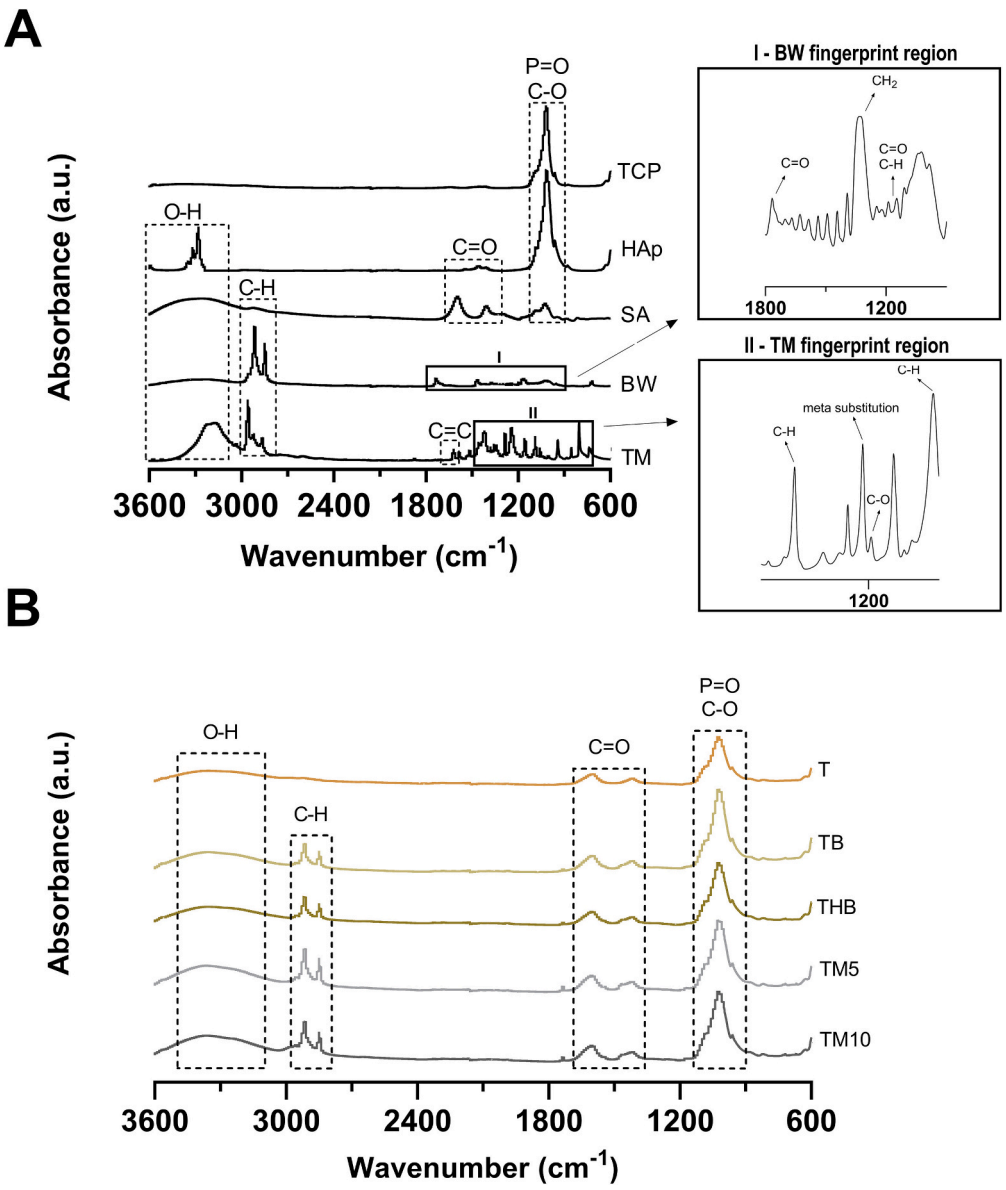

Fig. 2. ATR-FTIR analysis of raw materials (A) and T, TB, THB, TM5, and TM10 scaffolds (B).

for TB, THB, TM5, and TM10 (Fig. 3C). Particularly, in the wet state, the formulations containing BW maintained their energy absorption, whereas this value decreased from 1.35 ± 0.19 to 0.09 ± 0.01 MJ/m^3 for the T scaffolds. These show that the TB, THB, and TM formulations have superior fracture resistance and damage tolerance, in dry and wet states. Furthermore, there is also a noticeable increase in YM in wet conditions, but the addition of BW is unable to maintain YM within the trabecular bone range (50–2000 MPa). However, BW improved the scaffolds' plasticity in both conditions, as indicated in Fig. 3B. The YM of composite mixtures with BW showed an increase of more than 100 % compared to the control formulation in dry conditions, further enhancing T plasticity within trabecular bone values.

3.4. 3D scaffolds porosity evaluation

The total porosity of the scaffolds was measured using the liquid displacement method (Fig. 4A). The ability of cells to infiltrate, grow, and proliferate depends greatly on the pore size and interconnectivity, as this regulates cell movement, nutrient exchange, and metabolite diffusion within the scaffold structure. Additionally, pore interconnectivity facilitates the diffusion of ions such as Ca^{2+} and PO_4^{3-} throughout the scaffolds, leading to the formation of hydroxyapatite-like layers [60,70]. The results obtained for the scaffolds indicate that all the formulations fall within the range of trabecular bone porosity (50 %-90 %). Although this is a significant achievement, we can observe that when compared to the control formulation T (≈ 60.5 % porosity), the addition of BW (TB) reduces porosity by ≈ 10 % to 50.2 %. However, this effect is contradicted by the addition of HAp to the mixture (THB), as it increases total porosity to 63 %, a 3 % and 13 % increase compared to the control and TB, respectively. These results align with data available in the literature, where the BW has functioned as an occlusive agent and HAp is known to enhance scaffolds' inner porosity [60,71]. In addition, incorporating TM slightly increases the total porosity compared to TB (≈ 50.2 % porosity). TM5 and TM10 had porosity values of 52.5 % and 55 %, respectively, higher than the TB formulation, which can be explained by the presence of TM creating small spaces between the ceramic and polymer grains bonded by the BW. However, it still decreases porosity by 2.3–5.5 % when compared to the control T. Moreover, all composite mixtures resulted in 3D scaffolds with macro-porosity compatible with cell internalization, mean pore size within

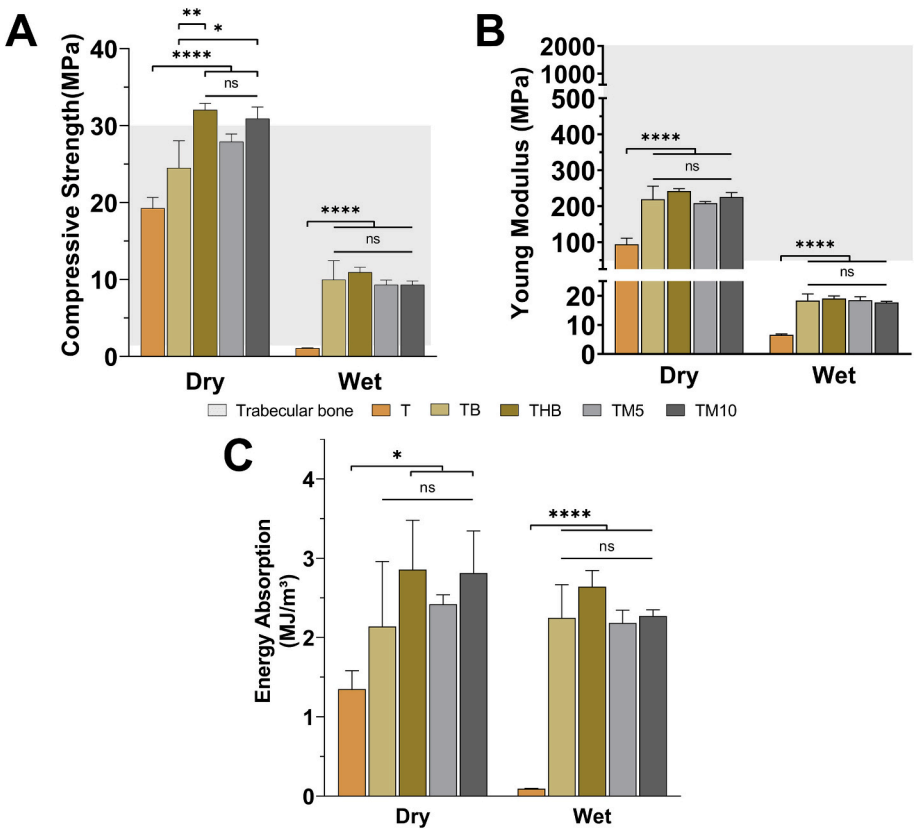

Fig. 3. Evaluation of the 3D scaffolds' Cs (A), YM (B), and Energy Absorption (C), under dry and wet conditions. Data are presented as mean ± standard deviation, $n = 3$, $^{*}p < 0.01$ and $^{****}p < 0.0001$; ns – not significant.

2063–2617 ± 250 μm and 205–605 ± 250 μm, as shown in Table S4, and SEM images (Fig. 4B).

3.5. Evaluation of the scaffolds' wettability

The hydrophobic/hydrophilic nature of the materials directly influences cell adhesion and protein absorption onto the scaffolds' surface. According to the literature, cell adhesion is more favorable on moderately hydrophilic surfaces (40° < WCA < 70°) when compared to hydrophobic surfaces (WCA > 90°) or super hydrophilic surfaces (WCA < 20°) [72]. The results show that the T formulation exhibited a superhydrophilic nature with a low contact angle of 4.5 ± 0.4°. In turn, the inclusion of BW improved the WCA of TB and THB formulations, increasing the hydrophobicity to 25.4 ± 1.2° and 26.8 ± 1.4°, respectively. These results are closer to the ideal range and align with those reported in the literature. The BW's hydrophobic nature is frequently mentioned in the Agro-Food industry as it is a valuable characteristic of emulsion production [73,74]. Subsequently, the TM5 and TM10 formulations containing a mixture of BW-TM demonstrated further improvement in the WCA (Fig. 4C). The hydrophobic nature of TM further increased the formulations' hydrophobic nature, reaching 45.6 ± 3.6° and 43.9 ± 0.4°, respectively. Therefore, TM5 and TM10 3D scaffolds present WCA values within the ideal range (40° < WCA < 70°) for promoting the cells' adhesion and proliferation, which can positively influence their biological performance.

3.6. Characterization of the scaffolds' swelling profile

When the scaffolds swell, their structure changes as the polymeric matrix expands, increasing pore sizes. This enables better cell penetration and nutrient diffusion throughout the scaffolds [52]. Nevertheless, excessive swelling can reduce the density of the scaffolds, leading to a loss of mechanical integrity and increasing the compressive stress on surrounding tissues [75]. The results showed that the T, TB, and THB formulations had similar swelling profiles when placed in the DMEM-F12 medium. Fig. 4D shows that all formulations present a rapid swelling in the first 4–5 h, which stabilized until the end of the experiment at 72 h. Moreover, T samples presented the highest swelling, with 420 % at 72 h. In turn, the BW inclusion resulted in 3D scaffolds with lower swelling, ≈15–20 % less for TB and THB formulations. The TM5 and TM10 3D scaffolds showed a more controlled swelling profile, with a peak swelling value of ≈280 % for TM5 and ≈240 % for TM10. The obtained results can be correlated with the data obtained in the porosity and WCA studies, i.e., lower porosity and increased hydrophobicity resulted in materials with a more controlled and lower swelling capacity. Therefore, these data show that including BW and TM in the composite mixture positively affects the 3D scaffolds' response to fluids, leading to more stable structures.

3.7. Evaluation of the scaffolds' mineralization capacity

The ability of scaffolds to promote mineral deposition is critical for bone tissue formation. During this process, the binding of calcium and phosphate ions facilitates the nucleation and growth of hydroxyapatite crystals ($Ca_5(PO_4)_3(OH)$) [76]. For that purpose, the scaffolds' mineralization was characterized for 21 days in SBF. The formation of apatite crystals on the scaffolds' surface was observed through SEM (Fig. 5A) and complemented with EDS analysis (Fig. 5B and C). The results show that during the first 3 days, the TB, THB, TM5, and TM10 formulations form fewer apatite crystals than the control T scaffolds (Fig. 5A). This observation was also confirmed by the lower amount of P and Ca elements found in these scaffolds (Fig. 5B and C) during the first 3 days. After this initial phase, a continuous deposition of apatite crystals occurred, and an increase in the P and Ca elements was observed until

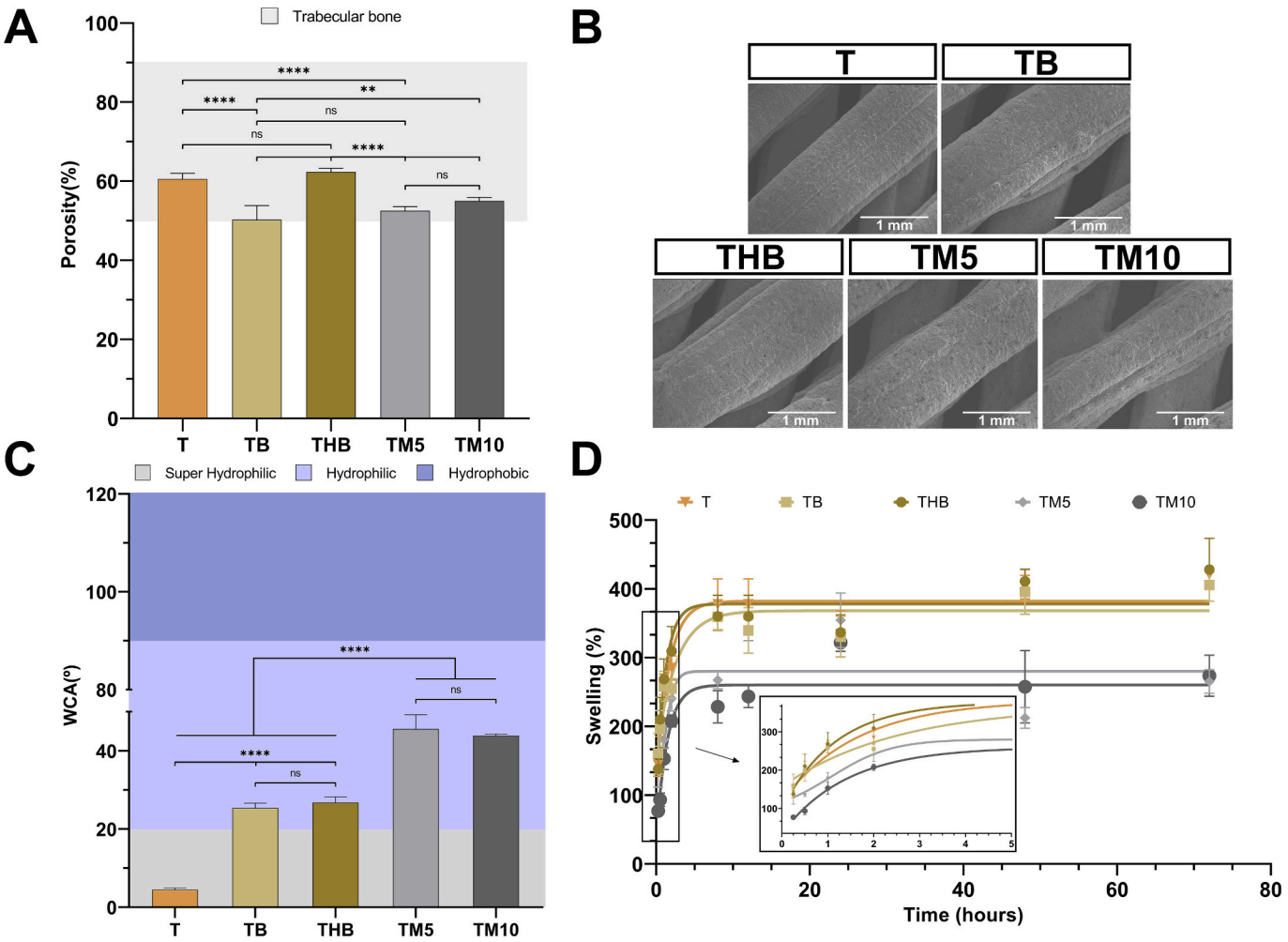

Fig. 4. Characterization of the scaffolds' total porosity (A); SEM images of the scaffolds' macroporosity (B); evaluation of the scaffolds' surface wettability (C); Analysis of the scaffolds' swelling profile (D). Data are presented as mean ± standard deviation $n = 5$, $^{**}p < 0.01$ and $^{****}p < 0.0001$; ns – not significant.

the end of the study. The results also show that the TM5 and TM10 formulations had the highest amounts of P and Ca elements after 21 days. Furthermore, the elemental surface map obtained using SEM on days 7 and 21 (Fig. S2) revealed a uniform distribution of both elements at the scaffolds' surface for all the formulations. Altogether, these data demonstrate that 3D scaffolds can trigger the mineralization process, creating a closer bone-like environment, which is crucial for supporting bone cell attachment, growth, and differentiation.

3.8. Evaluation of the scaffolds' biodegradation profile

The degradation rate of the scaffolds is a critical factor for guiding the formation of new tissue (Fig. S3). As temporary supports, the scaffolds must degrade at a rate that aligns with the new tissue formation to prevent mechanical instability [77]. Therefore, to assess the degradation profile of the scaffolds, they were incubated with DMEM-F12 medium in the presence or absence of lysozyme. Lysozyme is an enzyme typically found in saliva, macrophages, human serum, and neutrophil granules that mediates hydrolysis of *N*-acetyl glucosamine groups present in different materials, such as chitosan and peptidoglycans [52].

Based on the obtained results, it is possible to observe that the 3D scaffolds suffer a maximum degradation rate of 9 % over 14 days, both in the absence and presence of lysozyme (Figs. S3B and S3A). Moreover, most of the degradation occurs in the first 7 days, which can be attributed to the lack of specificity of the enzyme towards the different components present in the composite mixture and to the initial swelling that promotes the matrix expansion, creating space between the polymeric and ceramic phases. Additionally, the scaffolds with BW show a slightly faster degradation in the presence of lysozyme. Such can be related to the lysozyme capacity to promote a decrease of long, medium, and short-chain free fatty acids present in BW [78]. Moreover, it should be noted that upon implantation in the human body, the alginate lyases will also contribute to the 3D scaffolds' degradation through the cleavage of the glycosidic bonds between the sugar units [79]. Furthermore, the TCP and HAp can also undergo aqueous dissolution in body fluids and be reabsorbed and integrated into the mineralized bone tissue [80].

3.9. In vitro cellular characterization of the scaffolds

3.9.1. Assessment of hOB cells' viability and proliferation in contact with the scaffolds

The cytocompatibility of the 3D-printed composite scaffolds was analyzed in hOB cells for 21 days. For that purpose, the hOB cells were seeded and cultured in contact with the different 3D scaffold formulations. Optical microscopic images were obtained at various time points, and the collected images show the hOB cells with normal elongated morphology and proliferating until day 21 (Fig. S4). Moreover, these results were further corroborated by the resazurin assay. This assay explores the reduction of the nonfluorescent resazurin to the strongly fluorescent resorufin by living and metabolically active cells. Therefore, the obtained fluorescence will be proportional to the number of viable cells. Fig. 6A indicates that all formulations remained biocompatible

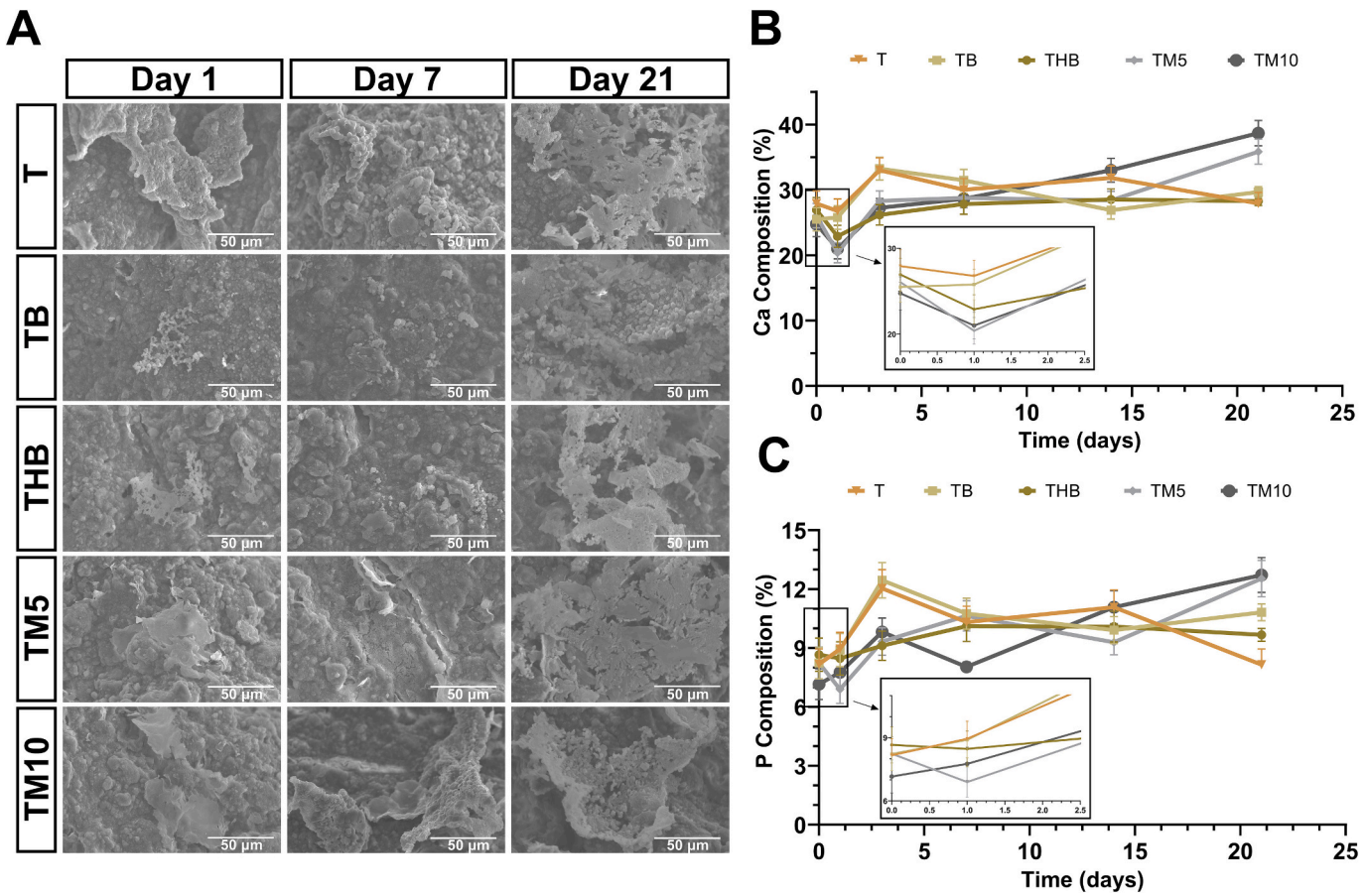

Fig. 5. Evaluation of in vitro mineralization of the 3D scaffolds. Apatite deposition representative SEM images onto the scaffolds' surface after incubation in SBF for 1, 7, and 21 days (A); EDS analysis of calcium (B) and phosphorous (C) atomic percentages on the scaffolds' surface.

over 21 days, with all tested formulations showing cellular viabilities superior to 70 %. Nevertheless, it is also possible to notice a slight decrease in the hOB cells' viability (to ≈80 %) when they were seeded in contact with the T 3D scaffolds, during the first 3 days. Otherwise, the incorporation of BW and TM in the 3D scaffolds did not impact the hOB cells, with the TB, THB, TM5, and TM10 formulations showing cellular viabilities of ≈100 % without significant differences to the K^- group. This cytocompatibility profile is aligned with previous reports in the literature [81,82]. Vu et al. reported that incorporating TM at different concentrations (500 μg and 1000 μg) into a hydroxyapatite-coated titanium implant maintained cell viability throughout an 11-day assay period [82]. Moreover, Pereira and colleagues demonstrated that BW multifunctional composites exhibited over 90 % cell viability during 72 h [81].

3.9.2. *Evaluation of cell adhesion and internalization*

Apart from the 3D scaffolds' cytocompatibility, the capacity of hOB cells to adhere and proliferate at the surface of the scaffolds was also assessed by SEM (Fig. 6B). The obtained images show that the hOB cells adhered and spread across the surface of the scaffolds from day 1 to day 7.

At day 7, formulations with BW (TB and THB) and formulations with BW and TM (TM5 and TM10) exhibited hOB cells with typical osteoblastic morphology as cells began to form continuous layers and establish connections between them. These results are consistent with the physicochemical properties revealed in the previous sections. The 3D scaffolds' surface roughness provides important anchorage points for the hOB cells' adhesion. Additionally, the wettability results indicated that TM5 and TM10 presented WCA values within the range considered ideal for promoting cell adhesion. In contrast, despite showing the adhesion and spreading of hOB cells, the T formulation did not show the same levels of cell density and typical osteoblastic morphology as the other formulations, further corroborating the results of the resazurin assay (Section 3.9.1). Fig. 6A shows that the T formulation results in lower cell viability on the first 3 days of the study, leading to less cellular density and adhesion in the 7-day assay presented in Fig. 6B.

The adhesion and internalization of hOB (Red) cells throughout the scaffolds (Blue) were also analyzed using CLSM (Fig. S5). The results indicate that cells can penetrate the scaffold in all formulations at each time point. Such capacity is correlated with the macropores (Fig. 4B), which facilitate the cells' migration to deeper regions of the 3D-printed scaffolds. Moreover, on the 7th day, it was possible to observe some cellular aggregates, which have been shown to improve osteogenesis [83].

3.9.3. *In vitro biomineralization*

The scaffolds' biomineralization capacity was evaluated using the ARS staining method, after removing the scaffolds cultured with hOB cells. The ARS binds specifically to calcium ions (Ca^{2+}), fixed by hOB cells, forming a red or orange complex that allows the visual detection of the mineralization process. Therefore, optical microscopic images were acquired to assess the hOB cells' matrix mineralization ability when cultured with the 3D scaffolds over 21 days (Fig. S6). The obtained images clearly show the cells' staining, indicating the presence of calcium deposits in cultured cells, which is a hallmark of bone formation. Moreover, it is possible to observe that the increase in scaffolds' incubation time leads to a stronger ARS staining and the appearance of several stained deposits. In this way, the optical microscopy images show the continuous deposition of calcium, which indicates the capacity to promote the mineralization of the extracellular matrix and new bone

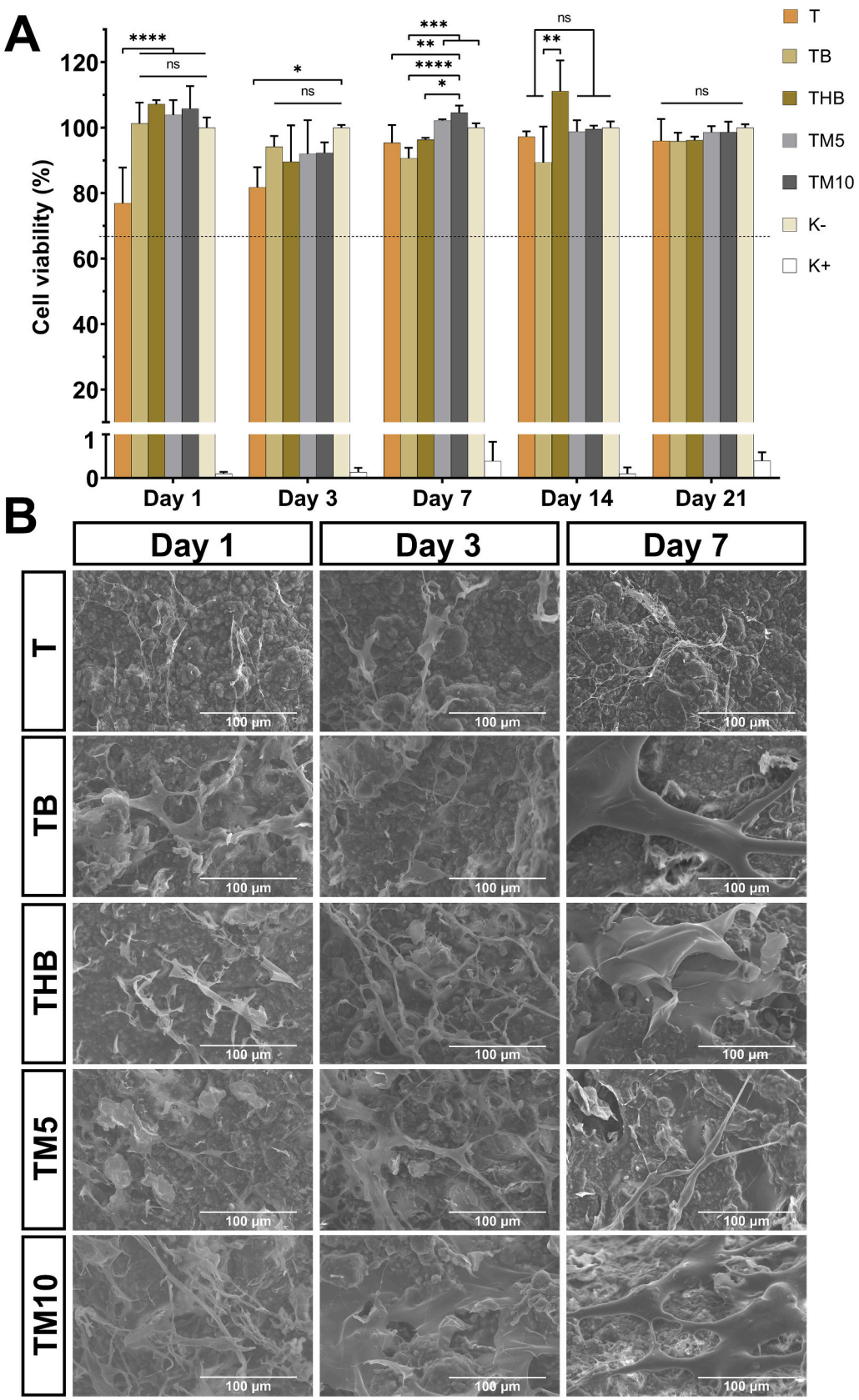

Fig. 6. Evaluation of the cellular viability profile at 1, 3, 7, 14, and 21 days of 3D scaffolds incubation with hOB cells. Positive control (K^+) -cells incubated with ethanol, and negative control (K^-) - cells cultured without the scaffolds. Data are presented as the mean ± standard deviation, $n = 5$; *$p < 0.01$ and ****$p < 0.0001$; ns – not significant (A). Representative SEM images of hOB cells adhered to the surface of 3D scaffolds at days 1, 3, and 7 (B).

formation. Furthermore, the higher number of calcium-rich deposits detected in the hOB cells incubated with TB, THB, TM5, and TM10 formulations reveals an apparent superior mineralization capacity. Such may be justified by the osteogenic properties of the materials and their capacity to promote the crystallization of calcium phosphate, as previously observed in Section 3.7 [84]. Similar findings were observed by Luo et al., showing that mineralized scaffolds (Alginate scaffolds coated with nano-HAp) enhanced the mechanical properties as well as the cell attachment and differentiation [85]. Moreover, it is worth noticing that the TB, THB, TM5, and TM10 formulations also presented physicochemical properties closer to those considered ideal for applications in BTE, further increasing their bioactivity, showing to be a clear advance over the previous scaffolds developed using TCP/SA-based composite mixtures [47,48,68].

3.9.4. Evaluation of the scaffolds' antibacterial activity

Hospital infections caused by bacteria are a severe complication associated with bone implants [52]. For that purpose, incorporating antibacterial agents into bone substitutes has been pursued for preventing bacterial infections. However, these agents should not compromise the osteoconductivity and osteoinductivity exhibited by scaffolds [86]. Hence, the antibacterial activity of the scaffolds was evaluated against two bacterial models, *S. aureus* (Gram-positive) and *E. coli* (Gram-negative), using the agar diffusion method. The results show that the groups treated with the T, TB, and THB formulations did not exhibit inhibition halos (Fig. S7). In turn, the adding TM to the composite mixtures demonstrated efficacy against both *S. aureus* and *E. coli*, as it presented inhibition halos within the standard values defined in the literature (Table S5) for the antibiotic gentamicin [87]. Moreover, both TM5 and TM10 3D scaffolds showed a higher inhibitory effect against *S. aureus*, a result consistent with the data available in the literature [28,65]. TM's mechanism of action involves permeabilizing and depolarizing bacterial membranes [88]. This permeabilization is easier in Gram-positive bacteria due to the outer peptidoglycan layer, which allows TM, a hydrophobic molecule, to penetrate. In contrast, this process is more difficult in Gram-negative bacteria, whose membranes are primarily composed of lipopolysaccharides that form a protective barrier against hydrophobic molecules, thereby reducing TM efficacy [28]. Moreover, it is worth noticing that the incorporation of BW would result in some degree of antibacterial activity [25]. However, the absence of inhibitory activity in TB and THB formulations may be attributed to the bleaching process undergone by the BW used in this work, which can lead to the depletion of bioactive compounds, such as propolis, responsible for these antibacterial effects. The resazurin assay also demonstrated strong antibacterial activity of TM scaffolds against *S. aureus* and *E. coli* (Fig. 7A and B), showing a significant reduction in metabolic activity to values close to those of the K^+. The analysis of the plates from the CFU study confirmed these results, indicating bactericidal effects of TM-containing scaffolds, without any detectable colonies in the TM5 and TM10 scaffolds (Fig. S8). Furthermore, SEM images (Fig. 8) also showed that the TM5 and TM10 successfully avoid the bacteria's adhesion and proliferation to the surface of the scaffolds, after 24 h of incubation with *S. aureus* and *E. coli*, consequently inhibiting the biofilm formation.

4. Conclusions

The addition of natural materials, i.e., BW and TM, resulted in the production of scaffolds with promising physicochemical, mechanical, and biological properties. The scaffolds containing BW showed improved mechanical properties, especially in humid conditions, without compromising their ability to absorb fluids and fix calcium and phosphate ions in the form of apatite crystals on the scaffolds' surface. In addition, BW also allowed the optimization of various physicochemical properties such as hydrophobicity and surface roughness, favoring cell growth. On the other hand, the incorporation of TM demonstrates the potential of this phenolic compound to be applied in tissue engineering solutions as a viable alternative to conventional antibiotic-based methods to prevent the establishment of bacterial infections and biofilm development. It is also important to note that, to the best of our knowledge, this is the first study to incorporate a mixture of BW and TM into the organic phase of 3D-printed scaffolds aimed at BTE. Nevertheless, additional assays are still required to validate the TM 3D scaffolds. For example, mechanical studies under bending and torsion loadings will provide additional information about the scaffolds' performance in a dynamic environment such as the human body. Scaffolds' osteoinductive capabilities should be further characterized using mesenchymal cells and monitored via ALP assays. In addition, in vivo assays will be

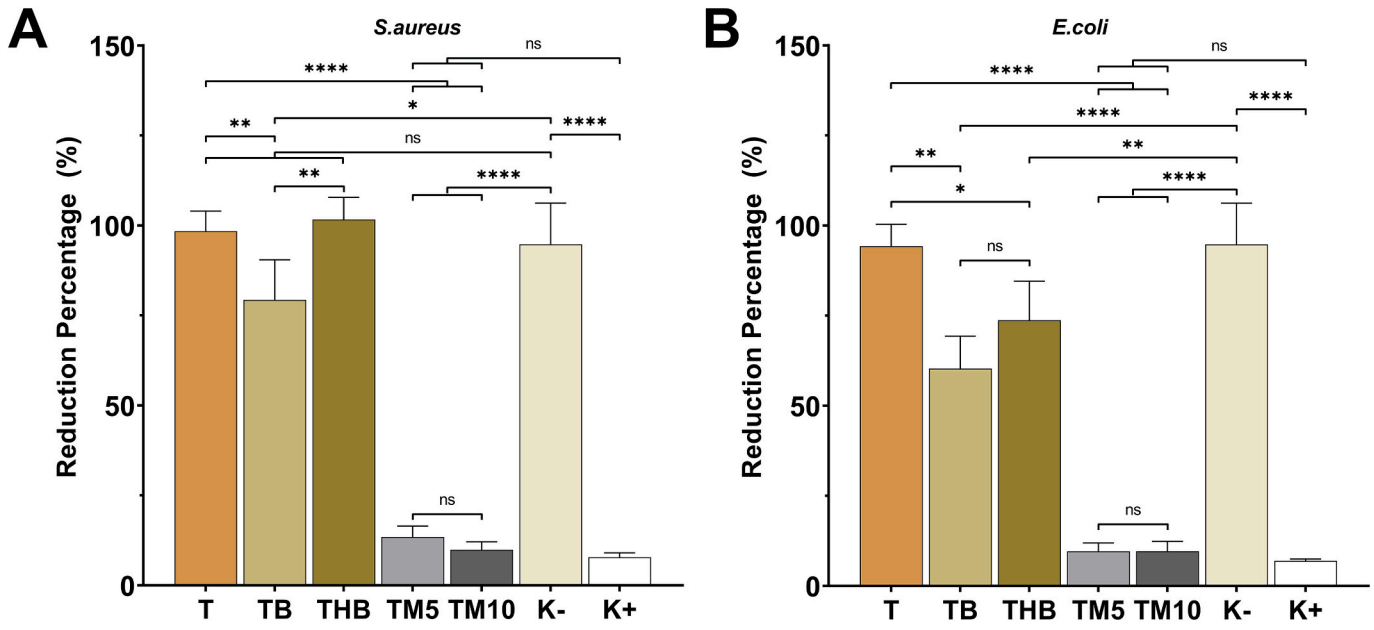

Fig. 7. Evaluation of *S. aureus* (A) and *E. coli* (B) metabolic activity upon 24 h incubation in the presence of the 3D scaffolds. Positive control (K^+) - bacteria incubated in LB media supplemented with antibiotic-antimycotic solution, and negative control (K^-) - bacteria cultured in media without the scaffolds. Data are presented as the mean ± standard deviation, $n = 5$; *$p < 0.01$ and ****$p < 0.0001$; ns – not significant.

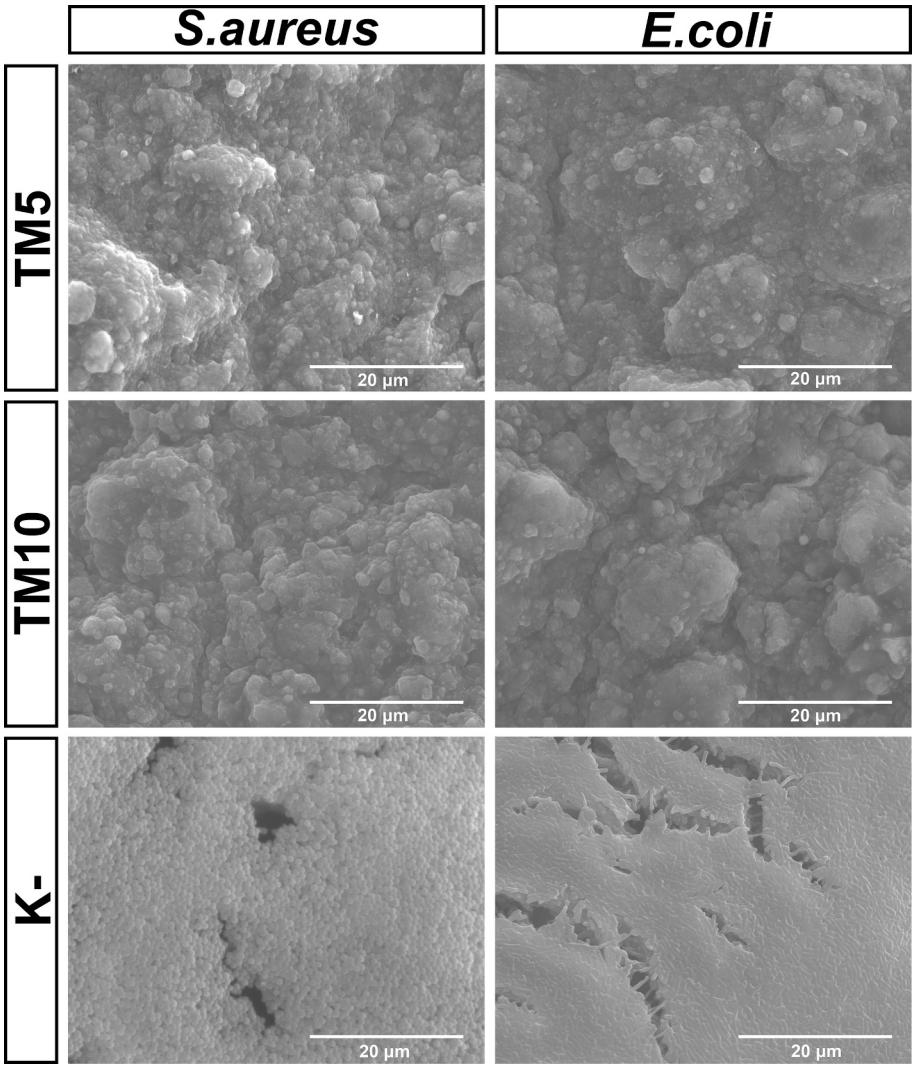

Fig. 8. Characterization of the antibacterial activity of the scaffolds. SEM images of the scaffolds' surface after being in contact with *S. aureus* and *E. coli* for 24 h.

essential to assess the potential of TM scaffolds for BTE applications.

CRediT authorship contribution statement

Martinho J. Francisco: Writing – original draft, Investigation, Formal analysis, Conceptualization. **Cátia S.D. Cabral:** Writing – review & editing, Investigation. **Paula Ferreira:** Investigation. **Ilídio J. Correia:** Writing – review & editing, Supervision, Funding acquisition. **André F. Moreira:** Writing – review & editing, Supervision, Funding acquisition, Conceptualization.

Declaration of competing interest

The authors declare that they have no known competing financial interests or personal relationships that could have appeared to influence the work reported in this paper.

Acknowledgments

The authors would like to thank Abílio Silva for the support in the mechanical assays. This work was developed within the scope of the CICS-UBI projects UIDB/00709/2020 and UIDP/00709/2020, financed by national funds through the Portuguese Foundation for Science and Technology/MCTES. The microscopy facility used in the development of this work is part of the PPBI-Portuguese Platform of BioImaging and is partially supported by the Project POCI-01-0145-FEDER-022122. Cátia S. D. Cabral is the recipient of a doctoral fellowship from FCT (UI/BD/151024/2021) under the scope of the CICS-UBI Programmatic Funding.

Appendix A. Supplementary data

Supplementary data to this article can be found online at https://doi.org/10.1016/j.bioadv.2025.214440.

Data availability

Data will be made available on request.

References

[1] S. Jagadale, M. Damle, M.G. Joshi, Bone tissue engineering: From biomaterials to clinical trials, in: K. Turksen (Ed.), Cell Biology and Translational Medicine, Volume 24: Regeneration in Normal and Cancerous Tissues, Springer Nature Switzerland, Cham, 2025, pp. 73–115.
[2] S.G. Pedrero, P. Llamas-Sillero, J. Serrano-López, A multidisciplinary journey towards bone tissue engineering, Materials 14 (17) (2021) 4896.
[3] W. Wang, K.W.K. Yeung, Bone grafts and biomaterials substitutes for bone defect repair: a review, Bioactive Materials 2 (4) (2017) 224–247.
[4] V. Campana, G. Milano, E. Pagano, M. Barba, C. Cicione, G. Salonna, W. Lattanzi, G. Logroscino, Bone substitutes in orthopaedic surgery: from basic science to clinical practice, J. Mater. Sci. Mater. Med. 25 (10) (2014) 2445–2461.
[5] I.H. Kalfas, Principles of bone healing, Neurosurgical Focus FOC 10 (4) (2001) 1–4.

[6] G.L. Koons, M. Diba, A.G. Mikos, Materials design for bone-tissue engineering, Nat. Rev. Mater. 5 (8) (2020) 584–603.
[7] K. Alvarez, H. Nakajima, Metallic scaffolds for bone regeneration, Materials 2 (3) (2009) 790–832.
[8] M.M. Stevens, Biomaterials for bone tissue engineering, Mater. Today 11 (5) (2008) 18–25.
[9] Ž. Perić Kačarević, P. Rider, S. Alkildani, S. Retnasingh, M. Pejakić, R. Schnettler, M. Gosau, R. Smeets, O. Jung, M. Barbeck, An introduction to bone tissue engineering, Int. J. Artif. Organs 43 (2) (2020) 69–86.
[10] B.Q. Le, V. Nurcombe, S.M. Cool, C.A. Van Blitterswijk, J. De Boer, V.L.S. LaPointe, The components of bone and what they can teach us about regeneration, Materials 11 (1) (2017) 14.
[11] B. Clarke, Normal bone anatomy and physiology, Clin. J. Am. Soc. Nephrol. 3 (Supplement_3) (2008) S131–S139.
[12] C. Soundrapandian, B. Sa, S. Datta, Organic–Inorganic Composites for Bone Drug Delivery, AAPS PharmSciTech 10 (4) (2009) 1158–1171.
[13] C.R. Lynch, P.P.D. Kondiah, Y.E. Choonara, Advanced strategies for tissue engineering in regenerative medicine: a biofabrication and biopolymer perspective, Molecules 26 (9) (2021) 2518.
[14] M.R. Cohn, A. Unnanuntana, T. Pannu, S.J. Warner, J.M. Lane, 7.16 Materials in Fracture Fixation, 2017.
[15] G. Turnbull, J. Clarke, F. Picard, P. Riches, L. Jia, F. Han, B. Li, W. Shu, 3D bioactive composite scaffolds for bone tissue engineering, Bioactive Materials 3 (3) (2018) 278–314.
[16] M.P. Nikolova, M.S. Chavali, Recent advances in biomaterials for 3D scaffolds: a review, Bioactive Materials 4 (2019) 271–292.
[17] C. Peteiro, Alginate production from marine macroalgae, with emphasis on kelp farming, Alginates and their biomedical applications (2018) 27–66.
[18] N.K. Sachan, S. Pushkar, A. Jha, A. Bhattcharya, Sodium alginate: the wonder polymer for controlled drug delivery, J. Pharm. Res. 2 (8) (2009) 1191–1199.
[19] A. Zheng, L. Cao, Y. Liu, J. Wu, D. Zeng, L. Hu, X. Zhang, X. Jiang, Biocompatible silk/calcium silicate/sodium alginate composite scaffolds for bone tissue engineering, Carbohydr. Polym. 199 (2018) 244–255.
[20] M.S.B. Reddy, D. Ponnamma, R. Choudhary, K.K. Sadasivuni, A comparative review of natural and synthetic biopolymer composite scaffolds, Polymers 13 (7) (2021) 1105.
[21] A. Silva-Barroso, C.S. Cabral, P. Ferreira, A.F. Moreira, I.J. Correia, Lignin-enriched tricalcium phosphate/sodium alginate 3D scaffolds for application in bone tissue regeneration, Int. J. Biol. Macromol. 239 (2023) 124258.
[22] S. Preethi Soundarya, V. Sanjay, A. Haritha Menon, S. Dhivya, N. Selvamurugan, Effects of flavonoids incorporated biological macromolecules based scaffolds in bone tissue engineering, Int. J. Biol. Macromol. 110 (2018) 74–87.
[23] K. Lavanya, K. Balagangadharan, S.V. Chandran, N. Selvamurugan, Chitosan-coated and thymol-loaded polymeric semi-interpenetrating hydrogels: an effective platform for bioactive molecule delivery and bone regeneration in vivo, Biomaterials Advances 146 (2023) 213305.
[24] C.D. Dumitru, I.A. Neacsu, A.M. Grumezescu, E. Andronescu, Bee-derived products: chemical composition and applications in skin tissue engineering, Pharmaceutics 14 (4) (2022) 750.
[25] F. Fratini, G. Cilia, B. Turchi, A. Felicioli, Beeswax: a minireview of its antimicrobial activity and its application in medicine, Asian Pac. J. Trop. Med. 9 (9) (2016) 839–843.
[26] R. Najafloo, N. Baheiraei, R. Imani, Synthesis and characterization of collagen/calcium phosphate scaffolds incorporating antibacterial agent for bone tissue engineering application, J. Bioact. Compat. Polym. 36 (1) (2021) 29–43.
[27] N. Gavaric, S.S. Mozina, N. Kladar, B. Bozin, Chemical profile, antioxidant and antibacterial activity of thyme and oregano essential oils, thymol and carvacrol and their possible synergism, Journal of Essential Oil Bearing Plants 18 (4) (2015) 1013–1021.
[28] S.P. Miguel, D. Simões, A.F. Moreira, R.S. Sequeira, I.J. Correia, Production and characterization of electrospun silk fibroin based asymmetric membranes for wound dressing applications, Int. J. Biol. Macromol. 121 (2019) 524–535.
[29] R. Najafloo, M. Behyari, R. Imani, S. Nour, A mini-review of thymol incorporated materials: applications in antibacterial wound dressing, J. Drug Deliv. Sci. Technol. 60 (2020) 101904.
[30] A.R. Ahmady, K. Razmjooee, S. Saber-Samandari, D. Toghraie, Fabrication of chitosan-gelatin films incorporated with thymol-loaded alginate microparticles for controlled drug delivery, antibacterial activity and wound healing: in-vitro and in-vivo studies, Int. J. Biol. Macromol. 223 (2022) 567–582.
[31] Z. Cui, X. Zhang, L. Zhou, W. Dong, Y. Wei, Z. Liu, X. Wu, A carrier-free injectable hydrogel self-assembled using natural thymol and glycyrrhizin for MRSA-infected wound healing in rats, Chem. Eng. J. 489 (2024) 151418.
[32] M. Zheng, Y. Huang, W. Hu, R. Li, J. Wang, M. Han, Z. Li, Evaluation of the antibacterial, anti-inflammatory, and bone-promoting capacity of UiO-66 loaded with thymol or carvacrol, ACS Appl. Mater. Interfaces 16 (28) (2024) 36017–36029.
[33] A. Hajibonabi, M. Yekani, S. Sharifi, J.S. Nahad, S.M. Dizaj, M.Y. Memar, Antimicrobial activity of nanoformulations of carvacrol and thymol: new trend and applications, OpenNano 13 (2023) 100170.
[34] C. Pavon, M. Aldas, J. López-Martínez, S. Ferrándiz, New materials for 3D-printing based on polycaprolactone with gum rosin and beeswax as additives, Polymers 12 (2) (2020) 334.
[35] Á. Aguilar-de-Leyva, V. Linares, M. Casas, I. Caraballo, 3D printed drug delivery systems based on natural products, Pharmaceutics 12 (7) (2020) 620.
[36] M. Martinello, F. Mutinelli, Antioxidant activity in bee products: a review, Antioxidants 10 (1) (2021) 71.
[37] Y. Nong, J. Maloh, N. Natarelli, H.B. Gunt, E. Tristani, R.K. Sivamani, A review of the use of beeswax in skincare, J. Cosmet. Dermatol. 22 (8) (2023) 2166–2173.
[38] F. Giampieri, J.L. Quiles, D. Cianciosi, T.Y. Forbes-Hernández, F.J. Orantes-Bermejo, J.M. Alvarez-Suarez, M. Battino, Bee products: an emblematic example of underutilized sources of bioactive compounds, J. Agric. Food Chem. 70 (23) (2022) 6833–6848.
[39] L. Cornara, M. Biagi, J. Xiao, B. Burlando, Therapeutic properties of bioactive compounds from different honeybee products, Front. Pharmacol. 8 (2017).
[40] J.M. Das, Bone wax in neurosurgery: a review, World Neurosurg. 116 (2018) 72–76.
[41] M. Salehiamin, H. Toolee, M. Azami, S.H.A. Tafti, S. Mojaverrostami, S. Halimi, S. Barakzai, A. Sobhani, Y. Abbasi, Chitosan scaffold containing periostin enhances sternum bone healing and decreases serum level of TNF-α and IL-6 after sternotomy in rat, Tissue Engineering and Regenerative Medicine 19 (4) (2022) 839–852.
[42] A. Izadyari Aghmiuni, S. Heidari Keshel, A. Aghababai, M. Zahraei, M. Rezaei-Tavirani, The design of natural hybrid biomaterial to promote osteogenic differentiation, collagen i and II expression and relief of musculoskeletal pains: bone tissue-engineering applications (in-vitro and clinical studies), Arab. J. Chem. 17 (6) (2024) 105766.
[43] N.K. Alruwaili, M. Rizwanullah, S.N. Abbas Bukhari, M. Amir, M.M. Ahmed, M. Fazil, 3D printing technology in design of pharmaceutical products, Curr. Pharm. Des. 24 (42) (2018) 5009–5018.
[44] A. Anawati, M.F. Fitriana, M.D. Gumelar, Improved corrosion resistance of magnesium alloy AZ31 in ringer lactate by bilayer anodic film/beeswax–colophony, Coatings 11 (5) (2021) 564.
[45] R. Fradique, T.R. Correia, S.P. Miguel, K. De Sa, D. Figueira, A. Mendonça, I. Correia, Production of new 3D scaffolds for bone tissue regeneration by rapid prototyping, J. Mater. Sci. Mater. Med. 27 (2016) 1–14.
[46] C. Wittkowske, G.C. Reilly, D. Lacroix, C.M. Perrault, In vitro bone cell models: impact of fluid shear stress on bone formation, Front. Bioeng. Biotechnol. 4 (2016) 87.
[47] T.R. Correia, D.R. Figueira, K.D. de Sá, S.P. Miguel, R.G. Fradique, A.G. Mendonça, I.J. Correia, 3D printed scaffolds with bactericidal activity aimed for bone tissue regeneration, Int. J. Biol. Macromol. 93 (2016) 1432–1445.
[48] A.S. Silva-Barroso, C.S.D. Cabral, P. Ferreira, A.F. Moreira, I.J. Correia, Lignin-enriched tricalcium phosphate/sodium alginate 3D scaffolds for application in bone tissue regeneration, Int. J. Biol. Macromol. 239 (2023) 124258.
[49] A.L. Torres, V.M. Gaspar, I.R. Serra, G.S. Diogo, R. Fradique, A.P. Silva, I.J. Correia, Bioactive polymeric–ceramic hybrid 3D scaffold for application in bone tissue regeneration, Mater. Sci. Eng. C 33 (7) (2013) 4460–4469.
[50] T. Kokubo, H. Takadama, How useful is SBF in predicting in vivo bone bioactivity? Biomaterials 27 (15) (2006) 2907–2915.
[51] J.C. Boga, S.P. Miguel, D. de Melo-Diogo, A.G. Mendonça, R.O. Louro, I.J. Correia, In vitro characterization of 3D printed scaffolds aimed at bone tissue regeneration, Colloids Surf. B Biointerfaces 165 (2018) 207–218.
[52] C.S.D. Cabral, S.P. Miguel, D. de Melo-Diogo, R.O. Louro, I.J. Correia, Green reduced graphene oxide functionalized 3D printed scaffolds for bone tissue regeneration, Carbon 146 (2019) 513–523.
[53] S.P. Miguel, M.P. Ribeiro, H. Brancal, P. Coutinho, I.J. Correia, Thermoresponsive chitosan–agarose hydrogel for skin regeneration, Carbohydr. Polym. 111 (2014) 366–373.
[54] B.P. Antunes, A. Moreira, V. Gaspar, I. Correia, Chitosan/arginine–chitosan polymer blends for assembly of nanofibrous membranes for wound regeneration, Carbohydr. Polym. 130 (2015) 104–112.
[55] C. Levard, S. Mitra, T. Yang, A.D. Jew, A.R. Badireddy, G.V. Lowry, G.E. Brown Jr., Effect of chloride on the dissolution rate of silver nanoparticles and toxicity to E. coli, Environ. Sci. Technol. 47 (11) (2013) 5738–5745.
[56] W.-C. Lin, C.-C. Lien, H.-J. Yeh, C.-M. Yu, S.-H. Hsu, Bacterial cellulose and bacterial cellulose–chitosan membranes for wound dressing applications, Carbohydr. Polym. 94 (1) (2013) 603–611.
[57] R. Fradique, T.R. Correia, S.P. Miguel, K.D. de Sá, D.R. Figueira, A.G. Mendonça, I. J. Correia, Production of new 3D scaffolds for bone tissue regeneration by rapid prototyping, J. Mater. Sci. Mater. Med. 27 (4) (2016) 69.
[58] L. Lin, K.L. Chow, Y. Leng, Study of hydroxyapatite osteoinductivity with an osteogenic differentiation of mesenchymal stem cells, J. Biomed. Mater. Res. A 89A (2) (2009) 326–335.
[59] C.S.D. Cabral, D. de Melo-Diogo, P. Ferreira, A.F. Moreira, I.J. Correia, Reduced graphene oxide–reinforced tricalcium phosphate/gelatin/chitosan light-responsive scaffolds for application in bone regeneration, Int. J. Biol. Macromol. 259 (2024) 129210.
[60] S.A.S. Nasrollah, N. Najmoddin, M. Mohammadi, A. Fayyaz, B. Nyström, Three dimensional polyurethane/ hydroxyapatite bioactive scaffolds: the role of hydroxyapatite on pore generation, J. Appl. Polym. Sci. 138 (11) (2021) 50017.
[61] A. Marchese, I.E. Orhan, M. Daglia, R. Barbieri, A. Di Lorenzo, S.F. Nabavi, O. Gortzi, M. Izadi, S.M. Nabavi, Antibacterial and antifungal activities of thymol: a brief review of the literature, Food Chem. 210 (2016) 402–414.
[62] A.R. Calore, V. Srinivas, L. Groenendijk, A. Serafim, I.C. Stancu, A. Wilbers, N. Leoné, A.A. Sanchez, D. Auhl, C. Mota, K. Bernaerts, J.A.W. Harings, L. Moroni, Manufacturing of scaffolds with interconnected internal open porosity and surface roughness, Acta Biomater. 156 (2023) 158–176.
[63] K. Rechendorff, M.B. Hovgaard, M. Foss, V.P. Zhdanov, F. Besenbacher, Enhancement of protein adsorption induced by surface roughness, Langmuir 22 (26) (2006) 10885–10888.

[64] L. Svečnjak, G. Baranović, M. Vinceković, S. Prđun, D. Bubalo, I.T. Gajger, An approach for routine analytical detection of beeswax adulteration using FTIR-ATR spectroscopy, J. Apicult. Sci. 59 (2) (2015) 37–49.
[65] A. Turki, E.O. Asma, M. Slah, Characterization and antimicrobial activity studies of Agave sheets with thymol and clove oil for active packaging, J. Nat. Fibers 20 (1) (2023) 2178583.
[66] P. Sotiropoulou, G. Fountos, N. Martini, V. Koukou, C. Michail, I. Kandarakis, G. Nikiforidis, Bone calcium/phosphorus ratio determination using dual energy X-ray method, Phys. Med. 31 (3) (2015) 307–313.
[67] C.F.L. Santos, A.P. Silva, L. Lopes, I. Pires, I.J. Correia, Design and production of sintered β-tricalcium phosphate 3D scaffolds for bone tissue regeneration, Mater. Sci. Eng. C 32 (5) (2012) 1293–1298.
[68] J.F.A. Valente, T.A.M. Valente, P. Alves, P. Ferreira, A. Silva, I.J. Correia, Alginate based scaffolds for bone tissue engineering, Mater. Sci. Eng. C 32 (8) (2012) 2596–2603.
[69] C. Liu, Z. Zheng, Y. Shi, Y. Zhang, Y. Liu, Development of low-oil emulsion gel by solidifying oil droplets: roles of internal beeswax concentration, Food Chem. 345 (2021) 128811.
[70] A. Mianehro, Electrospun bioscaffold based on cellulose acetate and dendrimer-modified cellulose nanocrystals for controlled drug release, Carbohydrate Polymer Technologies and Applications 3 (2022) 100187.
[71] C. Souza, L.A.P. de Freitas, P.M.B.G. Maia Campos, Topical formulation containing beeswax-based nanoparticles improved in vivo skin barrier function, AAPS PharmSciTech 18 (7) (2017) 2505–2516.
[72] S.M. Oliveira, N.M. Alves, J.F. Mano, Cell interactions with superhydrophilic and superhydrophobic surfaces, J. Adhes. Sci. Technol. 28 (8–9) (2014) 843–863.
[73] A. Shirvani, S.A.H. Goli, J. Varshosaz, L. Salvia-Trujillo, O. Martín-Belloso, Fabrication of edible solid lipid nanoparticle from beeswax/propolis wax by spontaneous emulsification: optimization, characterization and stability, Food Chem. 387 (2022) 132934.
[74] S.F. Hosseini, Z. Mousavi, D.J. McClements, Beeswax: a review on the recent progress in the development of superhydrophobic films/coatings and their applications in fruits preservation, Food Chem. 424 (2023) 136404.
[75] L. Tao, L. Zhonglong, X. Ming, Y. Zezheng, L. Zhiyuan, Z. Xiaojun, W. Jinwu, In vitro and in vivo studies of a gelatin/carboxymethyl chitosan/LAPONITE® composite scaffold for bone tissue engineering, RSC Adv. 7 (85) (2017) 54100–54110.
[76] H.C. Blair, Q.C. Larrouture, Y. Li, H. Lin, D. Beer-Stoltz, L. Liu, R.S. Tuan, L. J. Robinson, P.H. Schlesinger, D.J. Nelson, Osteoblast differentiation and bone matrix formation in vivo and in vitro, Tissue Eng. Part B Rev. 23 (3) (2017) 268–280.
[77] F.J. O'Brien, Biomaterials & scaffolds for tissue engineering, Mater. Today 14 (3) (2011) 88–95.
[78] A. Karaman, F. Yıldız-Akgül, N. Günay, Effect of different lysozyme treatments on the properties of Kashar cheese properties, Grasas Aceites 75 (1) (2024) e547.
[79] K.D. De Sá, D.R. Figueira, S.P. Miguel, T.R. Correia, A.P. Silva, I.J. Correia, 3D scaffolds coated with nanofibers displaying bactericidal activity for bone tissue applications, Int. J. Polym. Mater. Polym. Biomater. 66 (9) (2017) 432–442.
[80] J.G. Dellinger, A.M. Wojtowicz, R.D. Jamison, Effects of degradation and porosity on the load bearing properties of model hydroxyapatite bone scaffolds, J. Biomed. Mater. Res. A 77A (3) (2006) 563–571.
[81] R. Brito-Pereira, C. Ribeiro, C.R. Tubio, N. Castro, P. Costa, S. Lanceros-Mendez, Beeswax multifunctional composites with thermal-healing capability and recyclability, Chem. Eng. J. 453 (2023) 139840.
[82] A.A. Vu, S. Bose, Natural antibiotic oregano in hydroxyapatite-coated titanium reduces osteoclastic bone resorption for orthopedic and dental applications, ACS Appl. Mater. Interfaces 12 (47) (2020) 52383–52392.
[83] E. Lambertini, L. Penolazzi, A. Pandolfi, D. Mandatori, V. Sollazzo, R. Piva, Human osteoclasts/osteoblasts 3D dynamic co-culture system to study the beneficial effects of glucosamine on bone microenvironment, Int. J. Mol. Med. 47 (4) (2021) 57.
[84] Z. Bal, T. Kaito, F. Korkusuz, H. Yoshikawa, Bone regeneration with hydroxyapatite-based biomaterials, Emerg. Mater. 3 (4) (2020) 521–544.
[85] Y. Luo, A. Lode, C. Wu, J. Chang, M. Gelinsky, Alginate/nanohydroxyapatite scaffolds with designed core/shell structures fabricated by 3D plotting and in situ mineralization for bone tissue engineering, ACS Appl. Mater. Interfaces 7 (12) (2015) 6541–6549.
[86] K. Hayashi, M. Shimabukuro, K. Ishikawa, Antibacterial honeycomb scaffolds for achieving infection prevention and bone regeneration, ACS Appl. Mater. Interfaces 14 (3) (2022) 3762–3772.
[87] M.D. Mukhtar, F.A. Rufa'i, A.U. Yola, N.I. Babba, D. Baecker, Evaluating the Potency of Selected Antibiotic Medications Dispensed in Community Pharmacies in Gwale, Kano, Nigeria, Antibiotics 12 (11) (2023) 1582.
[88] J. Xu, F. Zhou, B.P. Ji, R.S. Pei, N. Xu, The antibacterial mechanism of carvacrol and thymol against Escherichia coli, Lett. Appl. Microbiol. 47 (3) (2008) 174–179.